Full-field strain reveals relaxation behaviors of main-chain liquid crystal elastomers in the polydomain-monodomain transition

J Van Blitterswyk[1,2], A.K. Landauer[1*], T.D. Nguyen[2*], C.M. Yakacki[3], A.M. Forster[1*]

[1]Material Measurement Laboratory, National Institute of Standards and Technology, 100 Bureau Dr., Gaithersburg, 20899, MD, USA.
[2]Department of Mechanical Engineering, The Johns Hopkins University, Baltimore, MD, USA.
[3]Department of Mechanical Engineering, University of Colorado Denver, Denver, CO, USA.

*Corresponding author(s). E-mail(s): alexander.landauer@nist.gov; vicky.nguyen@jhu.edu; aaron.forster@nist.gov;

Abstract

Background: Liquid crystal elastomers (LCEs) are polymers with nematic ordering that exhibit unique mechanical behaviors attributed to the interplay of network stretching and mesogen reorientation under loading. These competing viscoelastic mechanisms can lead to complex and heterogeneous local deformation response when exposed to an external stimulus such as light, thermal gradients, or applied stress. **Objective:** This study developed stereo digital image correlation (stereo-DIC) measurements and analyses of strain fields in polydomain LCE specimens undergoing the polydomain-monodomain (P-M) transition to reveal deformation mechanisms. **Methods:** Two macro-scale deformation modes probed the material response: quasi-static uniaxial extension and stepped stress-relaxation. Stereo-DIC tracked the full-field surface strain. A bespoke technique was developed consisting of a clustering algorithm to identify coherent strain clusters in the strain field at the maximum stress of the step loading and a stretched exponential model fit to the time-evolving strain response of the clusters and fitting to the stress relaxation response. This technique quantified differences in the viscoelasticity of the domains involved in the P-M transition. **Results:** Strain maps during the hold period showed that strain heterogeneity increased with time. Strain in the majority of clusters either increased asymptotically or decreased asymptotically with time, leading to increasing strain heterogeneity. The characteristic relaxation times varied between the clusters and were different from the that of the macroscopic stress response. **Conclusion:** A new technique for quantifying surface strain clustering is available. Initial findings on LCEs suggest that the kinematics of viscous mesogen rotation depends on the local strain state.

Keywords: liquid crystal elastomers, digital image correlation, full-field measurements, polydomain-monodomain transition, polymers, soft elasticity, viscoelasticity, stress relaxation, machine learning, clustering

1 Introduction

Liquid crystal elastomers (LCEs) are cross-linked polymer networks composed of flexible segments and anisotropic, rigid molecules, referred to as mesogens. Mesogens form well-ordered domains with spatially-varying orientations giving rise to features of both crystalline and rubbery materials [1]. Moreover, the mechanical properties can be tailored by synthesizing the networks with the mesogens in an isotropic state prior to cross-linking to give rise to a polydomain network, or with the mesogens aligned to give long-range order in a monodomain. The coupling between the liquid crystal (LC) order and the rubbery matrix gives rise to a phenomenon known as soft elasticity, where strain may increase without a proportional increase in stress in the global response of the polymer system [2]. The mobility of the mesogens allows them to rotate relative to the surrounding cross-linked network and align along the direction of maximum principal strain. Mesogen rotation accommodates large strains at zero stress (soft elasticity) or with little increase in stress (semi-soft elasticity). Under uniaxial stretching, this process occurs over a range of strains creating an extended plateau in the stress-strain response of the macro-scale material. Once mesogens are aligned in a monodomain, the material stiffens and behaves like a traditional cross-linked network [3–6]. This process is often termed the polydomain-monodomain (P-M) transition. The features of the stress-strain response and P-M transition depend strongly on orientation of the network during synthesis [5, 7–9], temperature [4, 6, 10–12], and loading rate [1, 13–15].

The soft-elastic phenomenon of LCEs is attractive for impact mitigation applications as a reversible energy dissipation mechanism [16, 17]. The relationship between mesogen order and applied stress with resultant changes in bulk mechanical properties has been studied extensively in the equilibrium regime [3–5, 8, 9, 13–15, 18–20], but there have been far fewer studies on non-equilibrium features, such as the slow stress relaxation [3, 6, 13, 18, 21]. Stress relaxation experiments have shown that the behavior of LCEs is complicated by the interaction of domain rotation and polymer chain relaxation mechanisms [5, 6, 13, 15, 21] and depends on many factors including the applied strain amplitude, synthesis history, mesogen order, network topology, and chemical structure, e.g., side-chain vs. main chain [13, 18, 22], strain rate [23], and loading condition [20]. In general, the relaxation behavior can be characterized by two domain time constants associated with fast and slow power-law relaxation, where the fast relaxation domain is generally related to direction changes in the nematic domains and the slow domain relates to network entanglements [13, 15]. Specifically, Ohzono *et al.* [21] showed that the hysteretic and relaxation behavior of LCEs depends strongly on the chemistry and strain history and is sensitive to local energy barriers due to the interaction of mesogens. Using stress-relaxation experiments at different levels of applied strain, Clarke & Terentjev [13] showed that the relaxation slows towards the onset of the P-M transition due to the elastic restraint on relaxation by neighboring domains as rotation first begins. A similar behavior was observed for side-chain LCEs in [18] where the relaxation time for isotropic polydomain nematic elastomers (PNEs) was considerably longer than nematic PNEs where the memory effect of the nematic synthesis acts to restore the original alignment more rapidly. These mechanisms may be used to inform designs for impact mitigation.

As a result of the sensitivity to local energy barriers caused by constraints from neighboring mesogenic groups and network structure, one would expect the relaxation response to be heterogeneous and complex throughout the P-M transition. This has been shown in many equilibrium studies where the deformation can become heterogeneous under uniaxial monotonic loading [6, 13–15, 21, 24, 25]. This heterogeneity in the local material response complicates the matter of using global stress and extension measurements for material modeling as this represents the aggregate response of many complex interactions. Therefore, the purpose of this work was to develop a full-field deformation measurement analysis that quantifies and uncovers the spatial and temporal heterogeneity of the relaxation across the PM transition in LCEs. To do so, we use incremental stress relaxation experiments to perturb the system from equilibrium at different levels of global strain to inform the kinematics of competing mechanisms (polymer stretching versus mesogen rotation) during relaxation. We also apply a clustering algorithm to the rich spatial strain measurements to quantify the variation in local relaxation responses across the gauge region. To the authors knowledge, this is one of a limited number of studies to use full-field measurements to characterize the response of LCEs [14, 24, 26] to mechanical stretching, and the first to leverage this for investigation of the stress relaxation response.

2 Materials and methods

2.1 Materials

Pentaerythritol tetrakis(3-mercaptopropionate) (PETMP), 2,2'-(Ethylenedioxy) diethanethiol (EDDET), 2,6 Di-tert-butyl-4-methylphenol (inhibitor), triethylamine (TEA), Phenylbis(2,4,6-trimethylbenzoyl)phosphine oxide (PPO), and toluene were purchased from Sigma-Aldrich (St. Louis, MO, USA)[1]. 2-Methyl-1,4-phenylenebis(4-(3-(acryloyloxy)propoxy)benzoate) (trade name RM 257) was purchased from Matrix Scientific (Columbia, SC, USA). All materials were used in as-received condition without further purification.

[1] Certain commercial equipment, instruments, software, or materials are identified in this paper in order to specify the experimental procedure adequately. Such identification is not intended to imply recommendation or endorsement by NIST, nor is it intended to imply that the materials or equipment identified are necessarily the best available for the purpose.

2.2 Specimen fabrication

All LCEs were synthesized using a one-stage thiol-acrylate Michael addition reaction as developed by Yakacki *et al.* [10, 27]. The LCE polymer networks were formed by combining acrylated-mesogen (RM 257) with 0.02 mol/mol of the inhibitor (rel. RM 257, EDDET and PETMP) and a mass fraction of 0.30 of toluene (rel. RM 257). The vial was then heated at 100 °C for approximately 15 min until the solution became clear, then mixed with a vortex mixer and reheated for about 5 min at 100 °C. Then, 0.90 mol/mol (rel. RM 257) of the di-functional thiol spacer (EDDET), 0.10 mol/mol tetra-functional cross-linker (PETMP) was added. The solution was mixed with a vortex mixer for ca. 30 s, and re-heated at approximately 100 °C until the solution became clear again. Next, 0.015 mol/mol of TEA (catalyst, rel. RM 257, EDDET and PETMP mixture) was added to the solution and mixed for approximately 30 s. The solution was then degassed under a partial vacuum of approximately -66 kPa gauge for about 30 s.

LCE sheets having a thickness of approximately 1 mm were made by pouring the solution between two glass molds separated by Teflon spacers. The plates were clamped together, covered in aluminum foil and left to cure for 24 hours at ambient laboratory conditions (ca. 23 °C and 30 % relative humidity). The molds were then placed in a heated vacuum chamber at approximately 100 °C for 12 h to remove excess toluene from the films. From the cured LCE sheet, specimens were cut using a razor blade into a rectangular shape approximately 65 mm by 10 mm by 1 mm.

2.3 Mechanical tensile testing

Uniaxial tension tests were performed in an electromechanical load frame with a calibrated 500 N force transducer (resolution 8.9 mN and ± 0.25 % nonlinearity error over the full scale range). Test specimens were clamped using spring loaded grips as shown in Fig. 1 with nominal gauge length between clamps of 45 mm. To compute the applied uniaxial stress, the width was computed at pixel resolution using a calibrated image of the specimen with approximately 0.037 mm/px resolution, and the thickness was taken as the mean of three measurements with a digital caliper (± 0.01 mm resolution) along the gauge length of each specimen. Expanded uncertainty on the stress measurement is ± 534 kPa. For a baseline understanding of the mechanical response and to identify the extension ratios over which the stress-plateau and P-M transition occurs, specimens were pulled to a stretch ratio ($\lambda = \frac{\text{final length}}{\text{initial length}}$) of approximately $\lambda_y = 2.5$ at a rate of 0.1 mm·s^{-1} (approximately 0.002 s^{-1}). Figure 3 shows a subset of this data. The specimens were thermally rejuvenated at 110 °C for 40 min and allowed to cool to ambient lab temperature before repeat testing.

Step-wise stress-relaxation experiments were then performed such that the stress plateau was traversed in six similarly-spaced increments in stretch (viz. $\lambda_{11} = 1.10$, 1.25, 1.39, 1.53, 1.68, 1.82). The specimen was pulled at a rate of 5 mm·s^{-1} (12.5 s^{-1}, roughly the highest rate attainable with this set up) to a given extension and allowed to relax for approximately 5 000 s before proceeding to the next extension without removal from the grips between each step. In each experiment the full-field time-dependent response of the specimen was measured using a stereo camera system and stereo digital image correlation (stereo-DIC) as described next.

Fig. 1: Snapshot of a speckled specimen mounted in spring loaded grips during a uniaxial test

2.4 Digital image correlation

Specimens were imaged during mechanical testing using two synchronized cameras (Blackfly S BFS-U3-51S5M-C, FLIR Inc); 2448 pixels by 2048 pixels, 10 bit monochrome, 3.45 μm square pixel size) with 50 mm F/2.8 adjustable focus and aperture lenses arranged relative to the specimen as depicted in Fig. 2. In general, the recommendations in the DIC Good Practices Guide [28] were followed during experiments. The cameras were calibrated with a stereo angle of approximately 17°, and a stand-off distance of approximately 475 mm. The specimen was illuminated using two light emitting diode (LED) arrays positioned at wide angles to the specimen to mitigate specular reflection and saturation. The camera system was calibrated using twelve stereo pairs of images of a calibration target positioned in various orientations within the shared field of view of the cameras, according to the vendor specifications for calibration. The calibration quality was verified using static and in-plane translations of a flat, speckled panel to ensure the intersection deviation and stereo residual in the center of the field of view were below 0.05 pixels and 1 pixel, respectively, over the center of the field of view (FOV). The calibrated FOV of the camera system was approximately 56 mm × 65 mm (height × width). For quasi-static tension experiments, synchronous image pairs were recorded at a rate of nominally 0.5 Hz. For stress relaxation experiments the rate was increased to

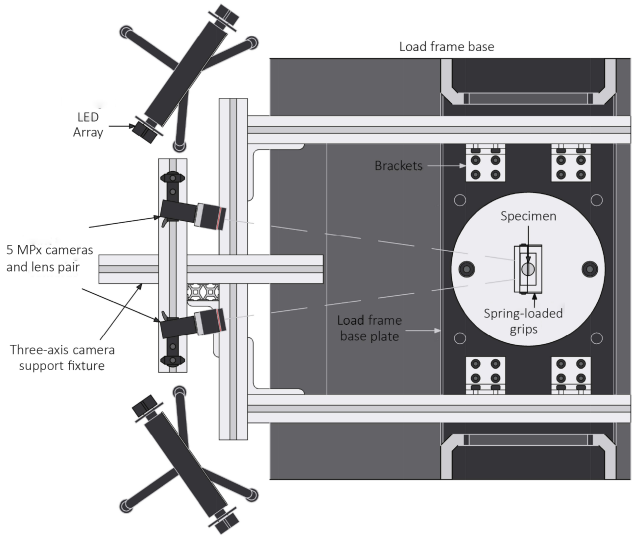

Fig. 2: Schematic of stereo camera system for 3D stereo digital image correlation (stereo-DIC). The cameras were arranged at about a 17° stereo angle on a fixed rail systems integrated with the load frame. LED light panels were placed on tripods at a wider stereo angle. The specimen was mounted in spring-loaded grips such that the wide face was orthogonal to the centerline of the stereo pair. The bottom grip is fixed and to top grip moves upward (out of the page) to impose stretch ratios greater than unity. Not drawn to scale.

5 Hz for the first 60 s of the test to capture the rapid relaxation response, after which the rate was reduced to 1 Hz for the remainder of the test.

The high extension ratio during the test complicates specimen preparation for DIC because the pattern becomes highly distorted, which negatively affects measurement performance. We attempted to reduce the distortion at high stretch ratios by speckling while the specimen is stretched. To do this, first the specimen is pre-stretched to a stretch ratio of about 1.5 and allowed to relax. The speckle pattern is then applied onto the substrate using an airbrush. Then the specimen is thermally reset by heating the unconstrained specimen at nominally 110 °C for 40 min, which is above the isotropic-nematic transition temperature. This removes mesogen ordering due to the initial stretch and allows for complete relaxation to the original undeformed configuration. Finally, the specimen is cooled at ambient laboratory conditions prior to testing.

Image pairs were correlated using GOM Professional (v. 2019) in incremental correlation mode (each image pair is correlated against the previous pair). The subset was set to 43 pixels (1.2 mm), with a step size of 11 pixels (0.3 mm). The subset was selected to be as small as feasibly possible to maximize the measurement spatial resolution across the gauge width while retaining sufficient features to maintain algorithm performance. Static images of the specimen were correlated and the standard deviation of displacement and strain components were used as estimates of the measurement uncertainty. A summary of the image correlation parameters and estimated measurement performance are provided in Table A2.

For quasi-static tests, every tenth image was selected for processing, whereas for stress relaxation experiments, images were chosen such that the logarithmic change in time (dt) between images was constant ($\log_{10}(dt) = 0.1$ decade). From each correlated image pair, we obtain the full-field (in-plane and out-of-plane) displacements of the front surface of the specimen. Due to the nature of subset-based image correlation algorithms, displacements within approximately one-half of a subset width from the edge of the specimen were excessively noisy and were discarded. The deformation gradient ($\mathbf{F}$) was computed from the displacement fields, $\mathbf{u}$, as $\mathbf{F} = \mathbf{I} + \nabla\mathbf{u}$, where $\mathbf{I}$ denotes the identity matrix and $\mathbf{u}$ denotes the displacement vector, and ∇ is the gradient operator. From $\mathbf{F}$ the in-plane components of the Green-Lagrange strain field were computed (E_{xx}, E_{yy}, E_{xy}) as, $\mathbf{E} = \frac{1}{2}(\mathbf{F}^T\mathbf{F}$ - $\mathbf{I})$. The in-plane rotation fields were computed through the polar decomposition of $\mathbf{F}$. Axial and lateral strains E_{yy} and E_{xx} are related to the axial stretch (λ_y) and lateral stretch (λ_x) as, $E_{yy} = \frac{1}{2}(\lambda_y^2 - 1)$ and $E_{xx} = \frac{1}{2}(\lambda_x^2 - 1)$.

3 Results, Analysis, and Discussion

3.1 Quasi-static stress response

The global stress-stretch curves at a strain rate of nominally 0.25 %·s^{-1} (0.1 mm·s^{-1}) for multiple nominally identical rectangular LCE specimens are shown in Figure 3. The mechanical response follows the expected behavior for polydomain main-chain LCEs [14], showing an initial viscoelastic response, a stress plateau (for these specimens this occurs between $0.1 \leq (\lambda - 1) \leq 0.6$), followed by a monotonic increase in stress with increasing stretch. The transverse strain response followed the anticipated $\lambda_{yy} = \lambda_{xx}^{-1/2}$ trend. Although the domains may differ between specimens the global response is remarkably similar. The full-field maps of axial, lateral and shear strains for six different extensions, roughly equally spaced across the stress plateau, are shown in Figure 4 for one example specimen.

Data in Figure 4 demonstrate that the global strains throughout the stress-plateau are generally homogeneous. At stage E, the specimen became optically transparent as the P-M transition was nearing its end. As reported in [14] the shear strains are below 10 % of the axial strains, although in this case the emergent heterogeneity in the axial strains appeared to be weaker. Here the axial strains were measured and plotted over the full gauge length, whereas in [14] strains were only measured over a small portion of the specimen, which may thus have higher resolution to capture subtle variations in the spatial response leading to more apparent heterogeneity.

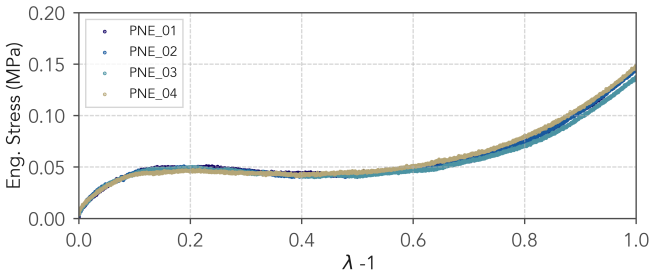

Fig. 3: Quasi-static stress-vs-strain repeats at 0.1 % s^{-1}

3.2 Incremental stress relaxation response

The PNE material specimen was thermally reset following the quasi-static experiments at nominally 110 °C for 40 min and allowed to cool to ambient lab temperature (approximately 23 °C). The specimen was then stretched uniaxially in a series of stress relaxation tests without removing the specimen from the grips. During the first stage ("A" in Fig. 4a) the specimen was stretched to approximately $\lambda = 1.10$ to investigate the relaxation response at the start of the stress-plateau. This was repeated at global stretches of $\lambda = 1.25$, 1.39, 1.53, 1.68, and 1.82 with the global stress relaxation curves at each state shown in Fig. 5.

The global relaxation behavior can be characterized by fitting a single stretched exponential function as described by a modified Kohlrausch-Williams-Watt (KWW) equation [22]:

$$\sigma(t) = (\sigma_{max} - \sigma_{min})\exp(-t/\tau)^{\beta} + \sigma_{min} \qquad (1)$$

The relaxation parameters τ and β are found by fitting a linear model to the relationship of $\ln[\ln[(1/R(t)]]$ versus $\ln(t)$, where $R(t)$ is the relaxation function defined as $R(t) = (E(t) - E_{min})/(E_{max} - E_{min})$ and E is the instantaneous global extension modulus (σ/e). This global fit for KWW provides a homogenized description of the overall behavior of the specimen. As a global measurement of a heterogeneous material this does not relate to specific material physics. However, once strain clustering is applied, the KWW fits to the subdomain clusters and carries physical meaning. From the linear regression, β, is equal to the slope, and describes the width of the relaxation spectrum. The relaxation time constant τ can be found from the y-intercept, which is equal to $-\beta\ln(\tau)$. The KWW fitting for each stage of relaxation is shown in Fig. B10 and a summary of relaxation parameters derived from each relaxation test are provided in Table 1. As was observed for main-chain smectic LCEs [22], nonlinear deviations emerge in the stretched exponential fit at short and long times. The β value varied between 0.20 and 0.26, which is substantially smaller than the 0.5 to 0.6 value typically measured for most conventional elastomeric networks. The small KWW exponent indicates a broad relaxation spectrum. There also exists a subtle but progressive narrowing of the exponential relaxation fitting as the specimen is extended through the P-M transition, as evidenced by the increase in β from 0.21

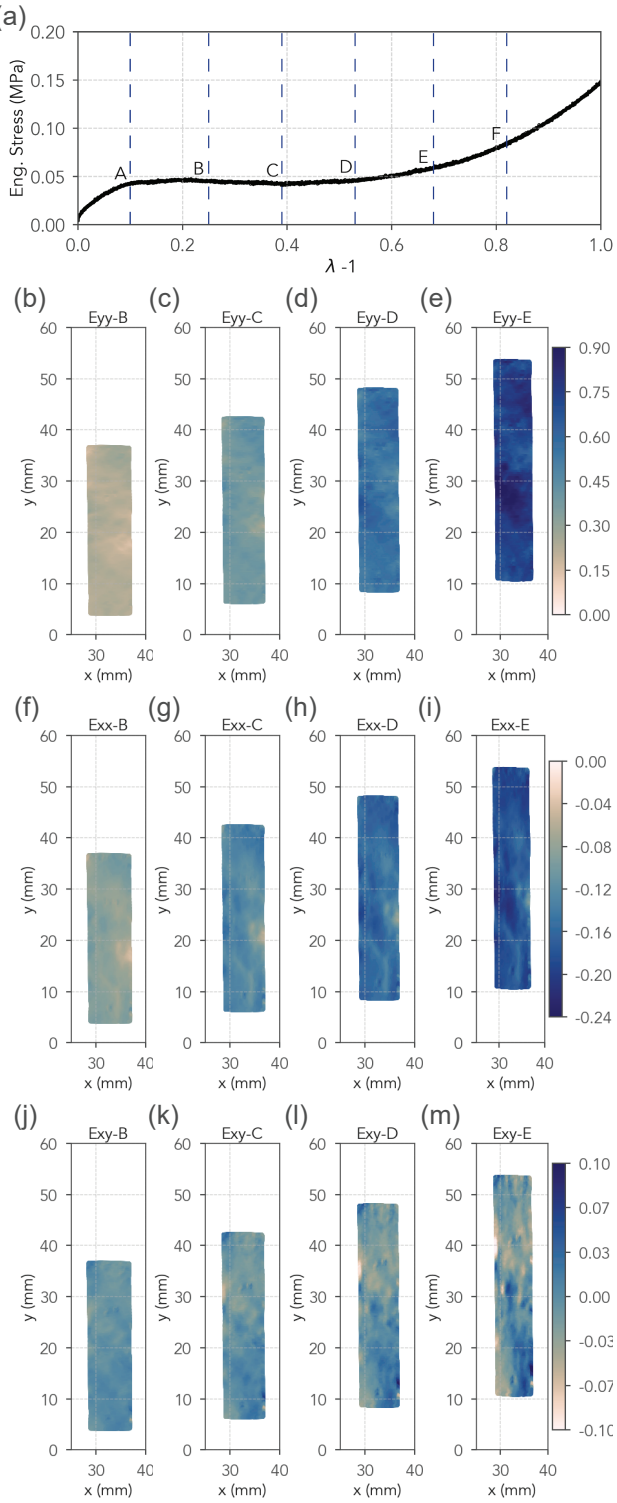

Fig. 4: Contour plots of full-field Green-Lagrange strain maps measured using stereo-DIC at four different extensions throughout the P-M transition at a loading rate of approximately 0.25 %·s^{-1}. The global quasi-static stress-stretch curve is shown in (a). The strain maps in (b)-(e) correspond to E_{yy}, (f)-(i) to E_{xx}, and (j)-(m) to E_{xy}. View in color for best clarity.

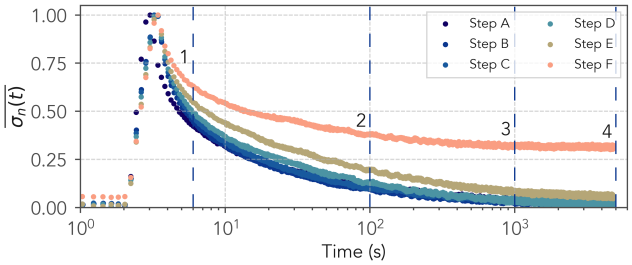

Fig. 5: Global stress relaxation curves for specimen an example PNE specimen at six different extensions. Note that the specimen was allowed to relax for 5 000 s between each increment. The stage letter in the legend denotes the global extensions in Fig. 4a and the numbers in each sub-plot indicate the time associated with the axial strain maps shown in Fig. 7.

at the start of the stress plateau to $\beta = 0.26$ at the end.

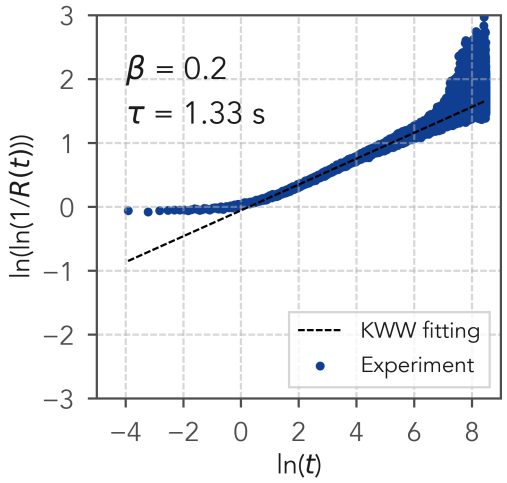

Fig. 6: Global stress relaxation fitting using modified KWW equation (Eq. 1) at a stretch state of $\lambda - 1 = 0.10$ (Step A) for an example specimen

Table 1: KWW parameters estimated from fitting the global stress relaxation across the P-M transition for an example specimen

Parameter	A	B	C	D	E	F
β	0.20	0.21	0.22	0.24	0.26	0.26
τ (s)	1.3	1.2	1.5	3.1	7.0	4.4

Substantial stress relaxation happens within the stress plateau, which occurs very slowly, similarly to [1, 15, 22]. The stress relaxes to near zero in the plateau, which indicates that the plateau stress may be caused by the viscous resistance to mesogen reorientation rather than the elastic semi-soft behavior of the anisotropic nematic state. This has been attributed to a complex relationship between changes in local nematic ordering that facilitates further relaxation that would not be possible in non-mesogenic polymer systems. It has been hypothesized that if local reorientation was able to occur, then preferential ordering within the specimen would impose a driving force on surrounding regions [1, 15, 22]. This would imply that the relaxation would proceed in a somewhat sequential manner, depending on the behavior of neighboring regions, potentially explaining the long-time stress relaxation response observed in the global response. However, global relaxation curves or local measurements of nematic order are largely unable to provide the measurement specificity needed to deconvolute this effect from other relaxation processes. Here, we attempt to investigate this indirectly using DIC to measure how the local surface strains vary to accommodate the almost full relaxation of stress through the P-M transition.

3.3 Full-field strain measurements during relaxation experiments

We examine the local behavior of the material using full-field DIC strain measurements throughout each stress relaxation experiment (see Sec. 2.4). As a summary, Fig. 7 shows the axial strain fields (E_{yy}) at four time points in the relaxation (1: 6 s, 2: 100 s, 3: 1 000 s and 4: 5 000 s) as indicated in global stress relaxation curves shown in Fig. 5. Note that strains are incremental relative to the first frame recorded for each step, and that the color scale varies from step to step to highlight the detail in each map.

The maps in Fig. 7 show a number of temporal and spatial behaviors to discuss. First, in all stages within the stress plateau ("B" to "E" in Fig. 4a) there is significant heterogeneity throughout the gauge region as the specimen approaches equilibrium. The variation in strain also changes as the stress plateau is traversed. For example, in stage B, we measure larger regions of high and low incremental strains along the length of the specimen (strains vary between 0.04 and 0.24 in Fig. 7h). As we continue stretching the material, the "texture" in the relaxed strain fields becomes more refined and pronounced towards the middle of the stress plateau (stages "C" and "D" - Figs. 7i-7p). Moreover, in stage D, the relaxed strain pattern seen in stage B (Figs. 7e-7h) has switched — what was relaxing to approximately zero incremental strain in B is now extending in D to relax out the stress. As the specimen is stretched past the stress plateau in stage F (Figs. 7u-7x) nearly all heterogeneity has disappeared and the strain settles near the applied global stretch as would be expected in a homogeneous continuum, which is how polymer networks are typically treated at this length scale.

To verify the observations, the same sequence of experiments was performed with the specimen rotated 180°, which confirmed that the patterns observed were not sensitive to proximity to the moving cross head, or the precise orientation within the grips. Specimen size was also varied and no sensitivity was observed, however edge effects are present. We also performed similar stepwise relaxation tests on elastomer tape (trade name VHB 4979, 3M, Saint Paul, MN, USA), as a non-mesogenic control material. A summary of the global stress relaxation curves are shown in Fig. B10 and a

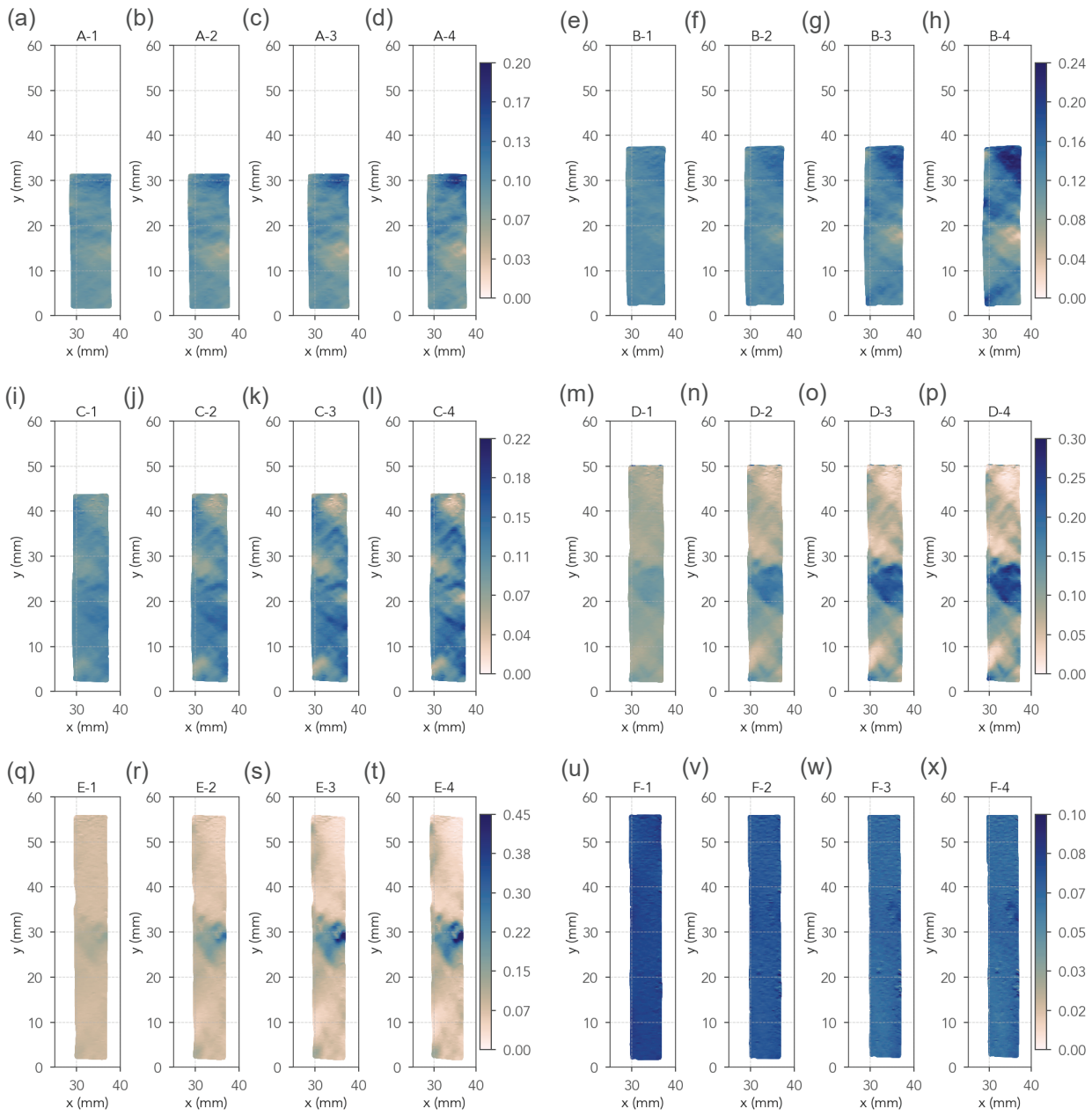

Fig. 7: Axial strain maps (E_{yy}) as measured using stereo-DIC during step-wise stress relaxation experiments at increasing axial extensions through the stress plateau. The strain maps in (a)-(d) correspond to "A" ($\lambda - 1 = 0.10$) in Fig. 4a, (e)-(h) to "B" ($\lambda - 1 = 0.25$), (i)-(l) to "C" ($\lambda - 1 = 0.39$), (m)-(p) to "D" ($\lambda - 1 = 0.53$), (q)-(t) to "E" ($\lambda - 1 = 0.68$), and (u)-(x) to "F" ($\lambda - 1 = 0.82$), respectively. Note that each test specimen was held for 5 000 s once the final global extension was reached. The numbers "1", "2", "3" and "4" in the title of each strain map corresponds to the time points highlighted in Fig. 5 at 6 s, 100 s, 1 000 s, and 5 000 s, respectively.

summary of measured strain maps in Fig. B11. Regardless of the initial stretch state, the full-field strain maps showed no appreciable heterogeneity as is expected for non-mesogenic, cross-linked polymer systems. Therefore, the specific textures measured in the LCE specimen relate to preferential local ordering in the microstructure, rather than specific experimental conditions. This is in contrast to the behavior of homogeneous viscoelastic polymers, e.g., see Fig. B10g, which has a markedly different characteristic relaxation.

The most noteworthy feature of the strain maps is the heterogeneity in the "relaxed" state at each stage takes the form of reasonably well-defined, neighboring regions of high and low incremental strain. This heterogeneous relaxation response is not immediately obvious in the global stress relaxation curves shown in Fig. 5. Moreover, the majority of strain evolution appears to occur at longer times. At stage F, and with the elastomer tape, the relaxation of strain related to the cross-linked network occurs quickly. Whereas, within the stress plateau, the strain fields continue to evolve slowly over long time periods. An additional test following stage B, where the specimen was allowed to relax overnight, indicates that the relaxation continues to evolve slowly for many hours after being stretched. This aligns with the theories proposed by [1, 15, 21, 22], which postulate that there is limited mobility between molecular chains, contributing

to the slow relaxation behavior tied to mesogen reorientation. Surface strain variation can be used as an indirect indicator of nematic re-ordering – as the material is stretched uniformly, the specimen deforms in a spatially heterogeneous way. To accommodate the reordering in a specific region, the surrounding areas experience local stresses that drive the specimen to collectively extend or contract within clusters to maintain the global extension constraints.

The ability to measure the full-field strain behavior across the specimen during the stress relaxation process provides unique and rich information about the competing mechanisms of mesogen reorientation and network relaxation. DIC shows that the relaxation response can be strongly heterogeneous and depends on the initial state from which the material is perturbed. While internal microstructural changes are not directly measurable from the surface-based DIC measurements, these maps provide valuable information about the distribution and character of the strain heterogeneity. This quantitative approach supplements the more qualitative but volume-averaged polarization-based (see for example the images in Fig. C13) approach. This could facilitate more targeted and informative microstructural measurements to quantify the relationship between microscale and macroscale changes in the material during relaxation in future.

3.4 Strain clustering to compare spatial relaxation behavior

We seek to quantify the spectrum of relaxation responses throughout the gauge region. To this end, we developed a new approach using a Bayesian Gaussian mixture model to cluster the strain fields by adopting the X and Y coordinates, and E_{xx} and E_{yy} as features. The coordinate values were scaled using standard scaling to normalize the feature space. The Gaussian mixture model approach was invoked due to the irregularity of the shape of regions identified in the relaxed strain maps, however this procedure requires a substantial amount of tuning. In future, more sophisticated clustering or additional feature engineering could improve the robustness and generalizability of the algorithm.

The final strain map collected during each stress relaxation experiment was used to train the clustering algorithm. The cluster assignments for all coordinates on the specimen were then tracked in time to monitor the evolution of strain within each region. The 'goodness' of the clustering is estimated by placing a threshold of 5 % on the normalized standard deviation (i.e., relative standard deviation or the standard deviation divided be the mean) of strain within each cluster. The number of clusters was then tuned manually such that approximately 60 % of the clusters had a normalized strain standard deviation of less than 5 %. This was found to be a good compromise between cluster refinement and sensitivity to measurement noise. As an example of this process, the 20 clusters identified from the last E_{yy} field in stage B is shown in Fig. 8a, from which the segregation of strain clusters into discrete domains is visible. The normalized standard deviation for each of the clusters is shown in Fig. 8b, with most clusters around or below the 5 % normalized standard deviation threshold. The E_{yy} distribution at each frame was then averaged (mean) and the evolution of mean strain was fit with a KWW model (Eq. 1) to extract the range of relaxation parameters across well-defined clusters within the gauge region. In this case instead of normalizing the instantaneous modulus, we normalize instantaneous E_{yy} as described in Eq. 1. This is shown for two representative clusters in Fig. 9. Note that complete data and example code to generate the strain histories, cluster maps, KWW fits and other plots are in the accompanying dataset published in the NIST Public Data Repository [29].

The data and fits in Figs. 9b and 9d show both cases following the stretched exponential distribution of the KWW model, as evidenced by the linearity of the response when plotted on a log scale to obtain the model parameters. For the cluster analysis, fit parameters were determined using a linear least squares regression fit to the approximate time range $t = [15, 2704]$ s, with β the slope and $\tau = \exp(-\beta/intercept)$. To apply Eq. 1, local stress on the cluster is needed. However, since only local strain is known the relaxation is instead computed on mean cluster strain E_{yy}, effectively normalizing to assume a constant σ throughout all clusters. In general, we observe three different relaxation behaviors within the strain clusters: first, decreasing strain, *e.g.*, Fig. 9a; second, increasing strain, *e.g.*, Fig. 9c; and, third, approximately constant strain within the recorded time frame. For clusters where strain increases in time, the stretched exponential has a broader spectrum with β values around 0.5 to 0.7, which is closer to a typical non-mesogenic polymer network (e.g., see Figure B10g). In contrast, the regions where strain decreases in time has a narrower spectrum, with β values typically between 0.7 and 1.5. In regions where the strain was approximately constant in time, the normalization in Eq. 1 was very small, and thus meaningful KWW fit parameters could not be computed.

The KWW fit is one way to quantify the relaxation response of the material. The full-field strain measurements show that the relaxation spectrum is quite broad across the gauge region and varies substantially from the global stress relaxation, which is described by a broader relaxation (Table 1). Generally, the global stress relaxation is characterized by the total response of two exponential functions, the parameters of which are used to infer differences in time scales between mesogen and network relaxation [13, 15, 23]. While observing similar behaviors in the strain response between clusters with increasing and decreasing strain over time, we are also able to investigate this on a local level. This enables identification of a much larger spectrum of relaxation behaviors within the specimen with more specificity and quantitation than is practical with polarization based techniques (see, for example, the plots in Figure C13 for comparison), as in, e.g., [4, 19, 25]. This technique could also be repeated for relaxation experiments from different initial states, temperatures or strain rates to

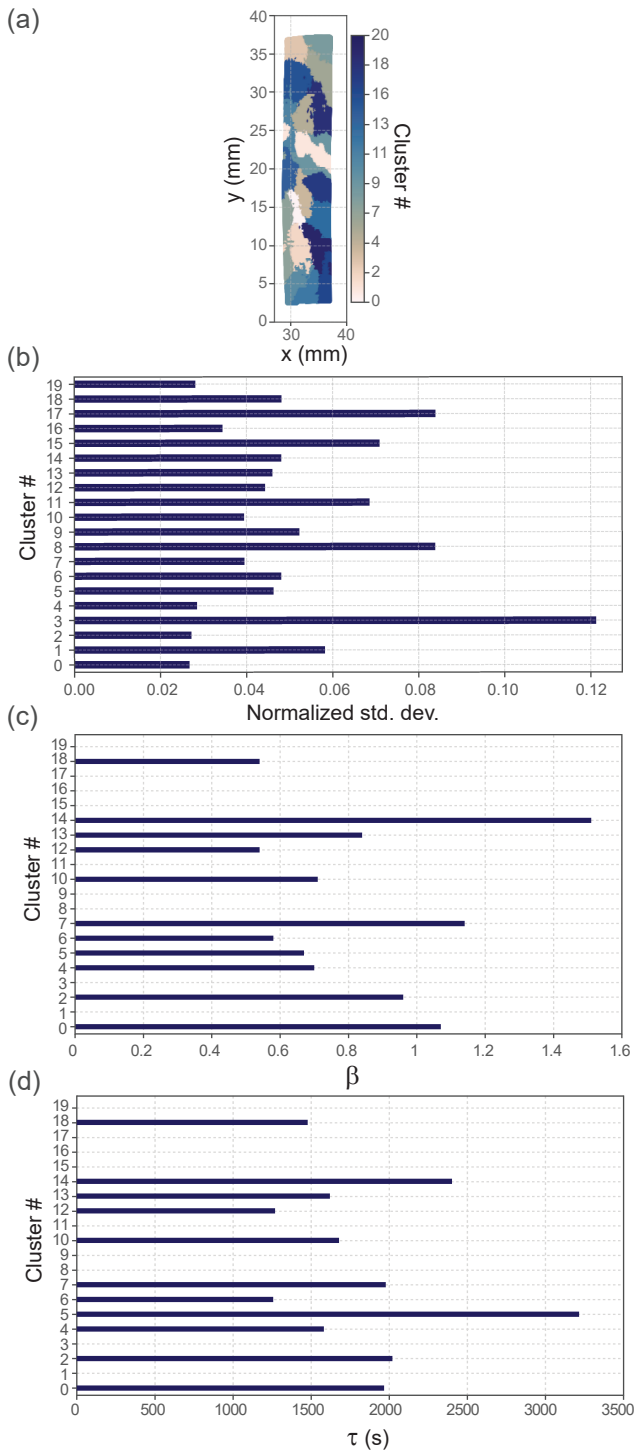

Fig. 8: (a) Clusters identified using a Gaussian mixture model trained on spatial coordinates and E_{xx} and E_{yy} strains as features. (b) Average standard deviation of strain normalized by mean cluster strain for all identified clusters. The "well-defined" clusters were identified by those which had a normalized standard deviation below 5 %. The strain in each cluster was averaged across each frame with the relaxation of the mean strain quantified using a modified KWW stretched exponential model. The relaxation parameters for each well-defined cluster are plotted in (c) β and (d) τ.

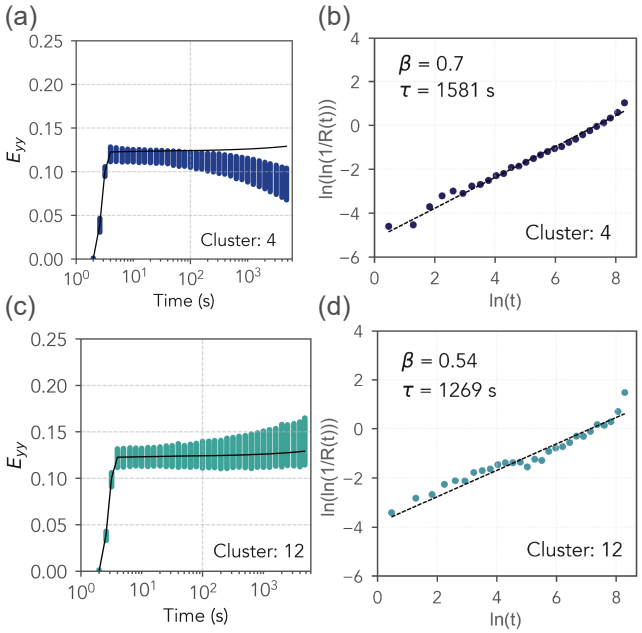

Fig. 9: Temporal evolution of E_{yy} strain and KWW fitting to mean cluster strain at each imaging frame for a representative cluster where strain decreases in time ((a),(b)) and a cluster where strain increases in time ((c),(d)). The solid line in (a) and (c) shows the mean cluster strain over the entire field of view. For (a) the blue data points highlight that cluster 4 relaxes substantially relative the mean strain whereas the green data points in (c) highlight that cluster 12 increases slightly. The dashed line (in (b) and (d) show the KWW linear regression used to obtain the parameters τ and β.

examine how the relaxation evolves as a function of global stretch. Moreover, the clustering algorithm identifies "transition" regions between clusters. Although outside the scope of this work, it would be particularly interesting to examine the microstructural features in these regions in an attempt to understand how neighboring regions interact and how this influences the final relaxation state.

4 Conclusions

In this study we demonstrated the use of full-field deformation measurements to densely sample the surface of a specimen, which can be used to quantify differences in local relaxation spectra for polydomain LCEs throughout the polydomain-monodomain transition. As the material was incrementally stretched through the P-M transition the surface strain maps showed reasonably well-defined regions within the specimen that behaved coherently in time. Using a custom machine learning-based clustering approach we showed that some regions extended as a function of relaxation time and other regions contracted. This is a new, direct measurement of the LCE domain transition accommodating local nematic re-ordering under a uniform external force. Once the P-M transition was complete, i.e. at large strains, the spatial distribution of strain was largely uniform, and the material behaved similarly to non-mesogenic cross-linked systems.

The machine learning framework developed was a Gaussian mixture model for clustering strain domains. It was used to automatically detect well-defined clusters across the surface of the specimen. The response of each cluster was characterized by fitting stretched exponential functions of a modified Kohlrausch-Williams-Watt form to the temporal evolution of strain. From these we measured a broad range of relaxation constants with β ranging from 0.5 to 1.5. Range of relaxation constants measured was empirically related to the nature of nematic reordering in the underlying material, i.e., contraction versus extension. The domains for isotropic genesis nematic elastomers have been measured to be between 1 micrometer to 10 micrometers. Therefore, the strains can vary through the thickness. Strain variations may, however, still exist and would not be specifically observable because the 3D-DIC technique only measures surface strain and the polarization technique averages the response through the thickness. These measurements highlight the complexity of the relaxation process in nematic LCEs, which cannot be adequately described using global stress relaxation measurements alone. The data from the measurements suggest that the strain evolution behavior is caused by mesogen reorientation that occurs at a local scale within the LCE, which is qualitatively observed via polarization and can be quantified with the clustering approach. The mesogen reorientation occurs at a large characteristic relaxation time and has a broader spectrum, as shown by how comparatively large beta is to the global LCE relaxation behavior. Furthermore, the spatial variation in beta and tau leads to an overall broad relaxation spectrum for the LCE compared to a homogeneous viscoelastic material.

This work highlights the utility of using DIC as a powerful tool for quantifying the heterogeneous relaxation response of LCEs throughout the polydomain-monodomain transition. The ability to measure the local response of the material creates many opportunities to develop advanced tests where spatial heterogeneity is intentionally controlled, providing more information from a single test. When combined with other measurement techniques that can assess local measurements of microstructural changes, this tandem of information could enhance efforts to characterize and model the kinetics of mesogen and network relaxation in LCEs.

Acknowledgments

The authors would like to thank Nick Traugutt and Risheng Zhou for assistance with sample preparation.

Declarations

Ethical Approval

Not applicable.

Consent to Publish

All authors have reviewed and approved the final manuscript.

Funding

T.D.N. acknowledges funding from the NSF CMMI program, award number 2437163.

Author Contributions

J.V.B., T.D.N., and A.M.F. conceptualized the study and all authors contributed to the study design. Material preparation, data collection and analysis were performed by J.V.B., A.K.L., and A.M.F. The draft of the manuscript was written by J.V.B. and expand and updated by A.K.L. All authors edited and commented on versions of the manuscript. All authors read and approved the final manuscript.

Competing Interests

The authors have no competing interests.

Disclaimers

These opinions, recommendations, findings, and conclusions do not necessarily reflect the views or policies of NIST or the United States Government.

Data Availability

The complete primary data along with minimum working example Python scripts to conduct the analysis are provided on the NIST Public Data Repository: https://doi.org/10.18434/mds2-3795.

References

[1] Terentjev, E.M., Hotta, A., Clarke, S.M., Warner, M.: Liquid crystalline elastomers: dynamics and relaxation of microstructure. Philosophical Transactions of the Royal Society A **361**, 653–664 (2003) https://doi.org/10.1098/rsta.2002.1155

[2] Warner, M., Bladon, P., Terentjev, E.M.: "Soft elasticity" — deformation without resistance in liquid crystal elastomers. Journal de Physique II **4**(1), 93–102 (1994) https://doi.org/10.1051/jp2:1994116 . Accessed 2024-04-12

[3] Fridrikh, S.V., Terentjev, E.M.: Polydomain-monodomain transition in nematic elastomers. Physical Review E **60**(2), 1847–1857 (1999)

[4] Clarke, S.M., Terentjev, E.M., Kundler, I., Finkelmann, H.: Texture evolution during the polydomain-monodomain transition in nematic elastomers. Macromolecules **31**, 4862–4872 (1998)

[5] Urayama, K., Kohmon, E., Kojima, M., Takigawa, T.: Polydomain-monodomain transition of randomly disordered nematic elastomers with different cross-linking histories. Macromolecules

42(12), 4084–4089 (2009) https://doi.org/10.1021/ma9004692

[6] Azoug, A., Vasconcellos, V., Dooling, J., Saed, M., Yakacki, C.M., Nguyen, T.D.: Viscoelasticity of the polydomain-monodomain transition in main-chain liquid crystal elastomers. Polymer **98**, 165–171 (2016) https://doi.org/10.1016/j.polymer.2016.06.022

[7] Traugutt, N.A., Volpe, R.H., Bollinger, M.S., Saed, M.O., Torbati, A.H., Yu, K., Dadivanyan, N., Yakacki, C.M.: Liquid-crystal order during synthesis affects main-chain liquid-crystal elastomer behavior. Soft Matter **13**(39), 7013–7025 (2017) https://doi.org/10.1039/c7sm01405h

[8] Higaki, H., Urayama, K., Takigawa, T.: Memory and development of textures of polydomain nematic elastomers. Macromolecular Chemistry and Physics **213**(18), 1907–1912 (2012) https://doi.org/10.1002/macp.201200239

[9] Kundler, I., Finkelmann, H.: Strain-induced director reorientation in nematic liquid single crystal elastomers. Macromolecular Rapid Communications **16**(9), 679–686 (1995) https://doi.org/10.1002/marc.1995.030160908

[10] Saed, M.O., Torbati, A.H., Nair, D.P., Yakacki, C.M.: Synthesis of programmable main-chain liquid-crystalline elastomers using a two-stage thiol-acrylate reaction. Journal of Visual Experiments **107**, 53546 (2016) https://doi.org/10.3791/53546

[11] Clarke, S.M., Tajbakhsh, A.R., Terentjev, E.M., Remillat, C., Tomlinson, G.R., House, J.R.: Soft elasticity and mechanical damping in liquid crystalline elastomers. Journal of Applied Physics **89**(11), 6530–6535 (2001) https://doi.org/10.1063/1.1368177

[12] Merkel, D.R., Traugutt, N.A., Visvanathan, R., Yakacki, C.M., Frick, C.P.: Thermomechanical properties of monodomain nematic main-chain liquid crystal elastomers. Soft Matter **14**, 6036 (2018) https://doi.org/10.1039/c8sm01178h

[13] Clarke, S.M., Terentjev, E.M.: Slow stress relaxation in randomly disordered nematic elastomers and gels. Physical Review Letters **81**(20), 4436–4439 (1998) https://doi.org/10.1103/PhysRevLett.81.4436 arXiv:9805382 [cond-mat]

[14] Martin Linares, C.P., Traugutt, N.A., Saed, M.O., Martin Linares, A., Yakacki, C.M., Nguyen, T.D.: The effect of alignment on the rate-dependent behavior of a main-chain liquid crystal elastomer. Soft Matter **16**(38), 8782–8798 (2020) https://doi.org/10.1039/d0sm00125b

[15] Hotta, A., Terentjev, E.M.: Long-time stress relaxation in polyacrylate nematic liquid crystalline elastomers. J. Phys.: Condens. Matter **13**, 11453–11464 (2001)

[16] Jeon, S.-Y., Shen, B., Traugutt, N.A., Zhu, Z., Fang, L., Yakacki, C.M., Nguyen, T.D., Kang, S.H.: Synergistic Energy Absorption Mechanisms of Architected Liquid Crystal Elastomers. Advanced Materials **34**(14), 2200272 (2022) https://doi.org/10.1002/adma.202200272

[17] Bischoff, A., Bawcutt, C., Sorkin, M., Yazzie, J., C. Cook, C., Leguizamon, S.C., Cook, A.W., Roach, D.J.: Monodomain Liquid-Crystal Elastomer Lattices for Broad Strain-Rate Mechanical Damping. Advanced Engineering Materials **27**(2), 2401796 (2025) https://doi.org/10.1002/adem.202401796

[18] Urayama, K., Honda, S., Takigawa, T.: Slow dynamics of shape recovery of disordered nematic elastomers. Physical Review E **74**(4), 041709 (2006) https://doi.org/10.1103/PhysRevE.74.041709

[19] Higaki, H., Takigawa, T., Urayama, K.: Nonuniform and uniform deformations of stretched nematic elastomers. Macromolecules **46**(13), 5223–5231 (2013) https://doi.org/10.1021/ma400771z

[20] Chung, C., Jiang, H., Yu, K.: Mesogen Organizations in Nematic Liquid Crystal Elastomers Under Different Deformation Conditions. Small **20**(47), 2402305 (2024) https://doi.org/10.1002/smll.202402305

[21] Ohzono, T., Katoh, K., Minamikawa, H., Saed, M.O., Terentjev, E.M.: Internal constraints and arrested relaxation in main-chain nematic elastomers. Nature Communications **12**(1), 787 (2021) https://doi.org/10.1038/s41467-021-21036-3

[22] Ortiz, C., K. Ober, C., Kramer, E.J.: Stress relaxation of a main-chain, smectic, polydomain liquid crystalline elastomer. Polymer **39**(16), 3713–3718 (1998) https://doi.org/10.1016/S0032-3861(97)10321-4

[23] Rezaei, L., Scalet, G., Peigney, M., Azoug, A.: Coupling between viscoelasticity and soft elasticity in main-chain nematic Liquid Crystal Elastomers. Journal of the Mechanics and Physics of Solids **187**, 105612 (2024) https://doi.org/10.1016/j.jmps.2024.105612

[24] Ware, T.H., Biggins, J.S., Shick, A.F., Warner, M., White, T.J.: Localized soft elasticity in liquid crystal elastomers. Nature communications **7**, 10871 (2016) https://doi.org/10.1038/ncomms10781

[25] Okamoto, S., Sakurai, S., Urayama, K.: Effect of stretching angle on the stress plateau behavior of main-chain liquid crystal elastomers. Soft Matter **17**, 3128–3136 (2021) https://doi.org/10.1039/

d0sm02244f

[26] Pritchard, R.H., Lava, P., Debruyne, D., Terentjev, E.M.: Precise determination of the Poisson ratio in soft materials with 2D digital image correlation. Soft matter **9**(26), 6037–6045 (2013)

[27] Yakacki, C.M., Saed, M., Nair, D.P., Gong, T., Reed, S.M., Bowman, C.N.: Tailorable and programmable liquid-crystalline elastomers using a two-stage thiol-acrylate reaction. RCS Advances **5**, 18997–19001 (2015) https://doi.org/10.1039/c5ra01039j

[28] Jones, E.M., Iadicola, M.A., et al.: A good practices guide for digital image correlation. International Digital Image Correlation Society **10** (2018)

[29] Van Blitterswyk, J., Forster, A.M., Landauer, A.K.: Full-field strain and force data and analysis for revealing relaxation behaviors of main-chain liquid crystal elastomers in the polydomain-monodomain transition. National Institute of Standards and Technology Public Data Repository (2025) https://doi.org/10.18434/mds2-3795

Appendix A DIC parameters

Typical DIC parameters for the experiments are given in Fig. A2.

Table A2: Digital image correlation parameters and measurement performance for LCE and VHB specimens

	Front
Speckle pattern	
Application technique	Manual, marker
Approx. feature size [px, mm]	81, 2
Grey level variation (σ) [%]	18
Mean grey level [%]	39
Image Correlation	
Interpolant	Bi-cubic spline
Shape function	Irregular
Maximum residual	10
Maximum intersection deviation [px]	0.10
Minimum pattern quality	0.60
Displacement calculation	
Image scale [mm·px^{-1}]	0.0275
Subset size, SS [px, mm]	43, 1.18
Step size, ST [px, mm]	11, 0.30
Edge data reconstruction	None
Smoothing window	None
Smoothing window σ [px, mm]	5, 0.122
Smoothing window width, SW (6σ) [px, mm]	30, 0.735
Strain calculation	
Formulation	Green-Lagrange
Displacement gradient calculation	Central difference
Edge data reconstruction method	None
Virtual strain gauge size ((SW-1)ST + SS) [px, mm]	86, 2.107
Measurement uncertainties	
u_x [px, μm]	0.010, 0.27
u_y [px, μm]	0.006, 0.16
u_z [px, μm]	0.047, 1.27
ϵ_{xx} [μm·mm^{-1}]	400
ϵ_{yy} [μm·mm^{-1}]	333
γ_{xy} [μm·mm^{-1}]	264

Appendix B Stress relaxation

This Appendix include additional plots showing stress relaxation experiments as R(t) vs ln(t) with global KWW fitting (Fig. B10), global stress relaxation at different axial extensions as $\overline{\sigma_n(t)}$ vs time (Fig. B11), and axial strain maps on a nominally homogeneous elastomer tape (Fig. B12).

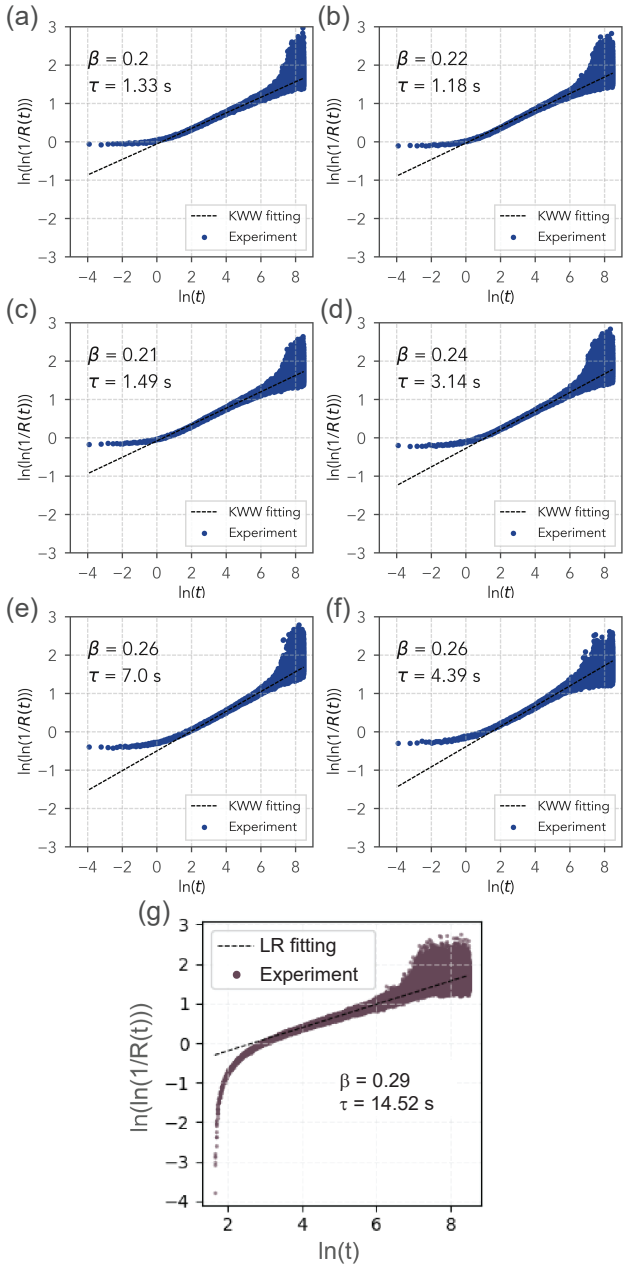

Fig. B10: Global stress relaxation fitting using modified KWW equation (Eq. 1) at each incremental stretch state: (a) $\lambda - 1$: 0.10, (b) $\lambda - 1$: 0.25, (c) $\lambda - 1$: 0.39, (d) $\lambda - 1$: 0.53, (e) $\lambda - 1$: 0.68, and (f) $\lambda - 1$: 0.82. For comparison, (g) shows a analogous example on a commercially available homogeneous viscoelastic material following the same protocol with linear regression (LR) fitting, corresponding to Fig. B11.

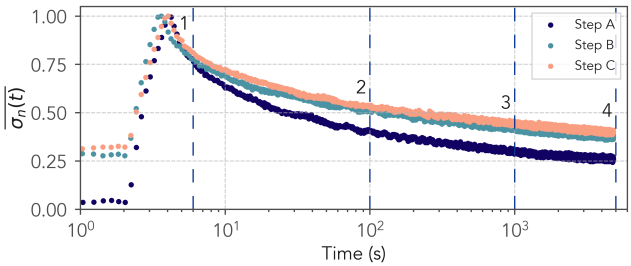

Fig. B11: Global stress relaxation curves for a representative specimen at three different extensions. Note that the specimen was allowed to relax for 5 000 s between each increment. The stage letter in the legend denotes the global extensions in Fig. B12a and the numbers in each sub-plot indicate the time associated with the axial strain maps shown in Figs. B12b-B12m.

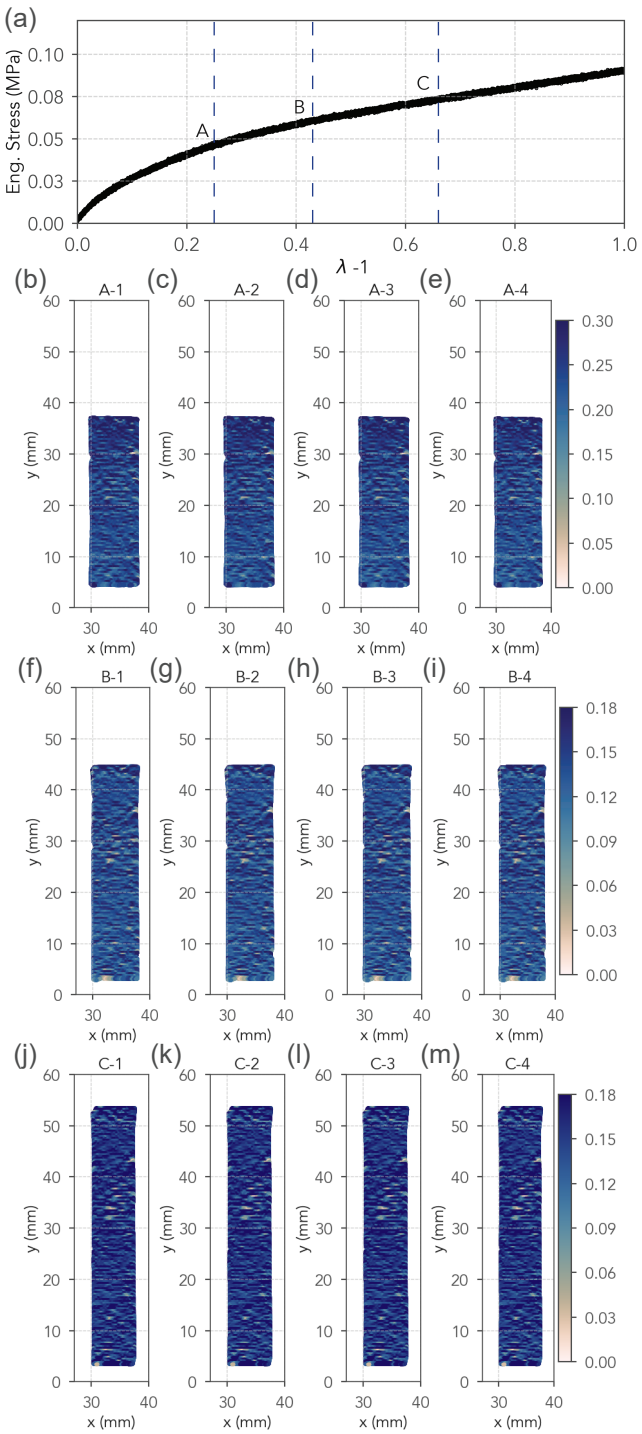

Fig. B12: Axial strain maps (E_{yy}) as measured using stereo DIC during stress relaxation experiments on an elastomer tape specimen performed step-wise at increasing axial extensions through the stress plateau. The quasi-static stress-stretch curve is shown in (a). The strain maps in (b)-(e) correspond to 'A' ($\lambda - 1$: 0.24), (f)-(i) to 'B' ($\lambda - 1$: 0.42), and (j)-(m) to 'C' ($\lambda - 1$: 0.64), respectively. Note that in each test the specimen was held for 5 000 s once the final global extension was reached. The numbers '1', '2', '3' and '4' on each strain map corresponds to the points in Fig. B11 at 6 s, 100 s, 1 000 s, and 5 000 s, respectively.

Appendix C Polarized imaging

A transilluminated polarized light configuration was also imaged and processed, see Fig. C13.

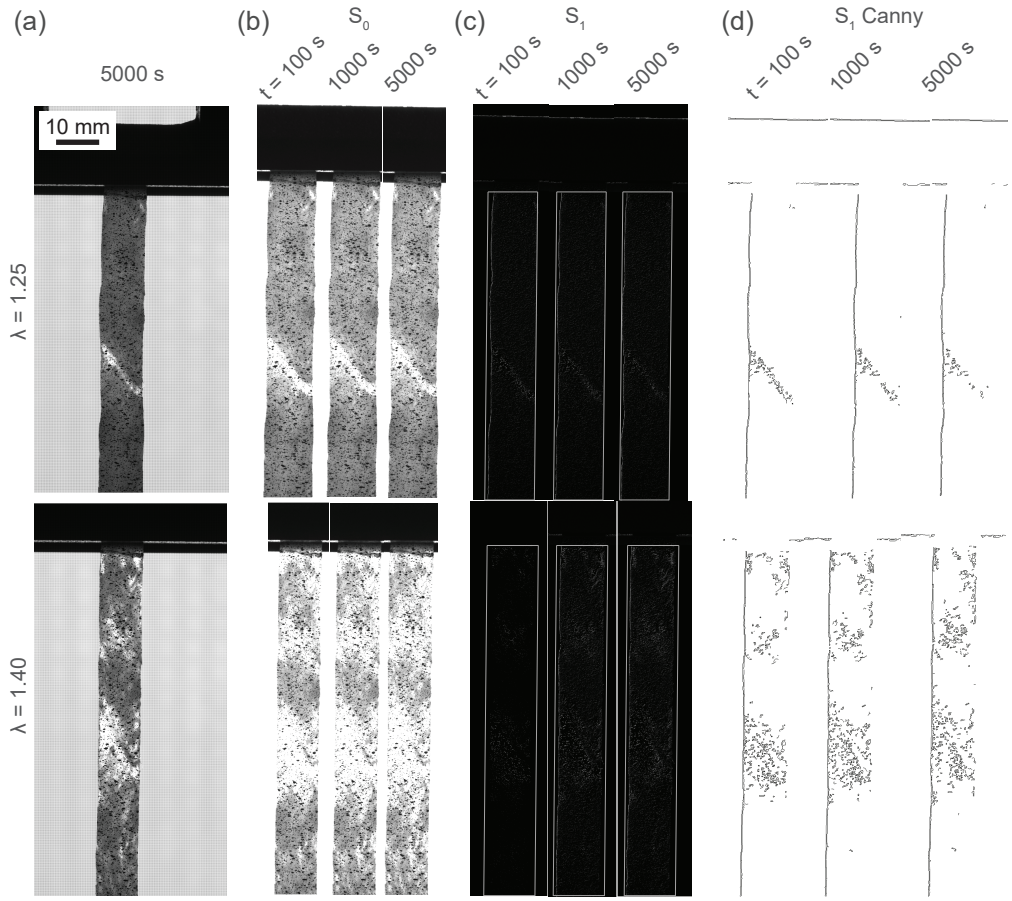

Fig. C13: Polarization-based images of an example tension relaxation experiment. (a) The specimen was transilluminated with linearly polarized light and the image was recorded on a sensor with polarized filter for each pixel at $I = 0°$, $I = 45°$, $I = 90°$, and $I = 135°$. Stoke's parameters were computed as (b) $S_0 = I_0 + I_{90}$, and (b) $S_1 = I_0 - I_{90}$. (d) To highlight differences a Canny edge filter is also applied on the S_1 image.